Miniaturized magnet-less RF electron trap. II. Experimental verification

Shiyang Deng[a)] and Scott R. Green[b)]
Center for Wireless Integrated MicroSensing and Systems (WIMS^2), University of Michigan, Ann Arbor, Michigan 48109

Aram H. Markosyan[c)] and Mark J. Kushner[d)]
Electrical Engineering and Computer Science Department, University of Michigan, Ann Arbor, Michigan 48109

Yogesh B. Gianchandani[e)]
Center for Wireless Integrated MicroSensing and Systems (WIMS^2), University of Michigan, Ann Arbor, Michigan 48109

Atomic microsystems have the potential of providing extremely accurate measurements of timing and acceleration. However, atomic microsystems require active maintenance of ultrahigh vacuum in order to have reasonable operating lifetimes and are particularly sensitive to magnetic fields that are used to trap electrons in traditional sputter ion pumps. This paper presents an approach to trapping electrons without the use of magnetic fields, using radio frequency (RF) fields established between two perforated electrodes. The challenges associated with this magnet-less approach, as well as the miniaturization of the structure, are addressed. These include, for example, the transfer of large voltage (100–200 V) RF power to capacitive loads presented by the structure. The electron trapping module (ETM) described here uses eight electrode elements to confine and measure electrons injected by an electron beam, within an active trap volume of $0.7 \, \text{cm}^3$. The operating RF frequency is 143.6 MHz, which is the measured series resonant frequency between the two RF electrodes. It was found experimentally that the steady state electrode potentials on electrodes near the trap became more negative after applying a range of RF power levels (up to 0.15 W through the ETM), indicating electron densities of $\approx 3 \times 10^5 \, \text{cm}^{-3}$ near the walls of the trap. The observed results align well with predicted electron densities from analytical and numerical models. The peak electron density within the trap is estimated as ~ 1000 times the electron density in the electron beam as it exits the electron gun. This successful demonstration of the RF electron trapping concept addresses critical challenges in the development of miniaturized magnet-less ion pumps. © 2017 American Vacuum Society. [http://dx.doi.org/10.1116/1.4984752]

I. INTRODUCTION

For microsystems that require very long-term control over package pressure, active on-board maintenance of pressure is an attractive complement to passive gettering.[1] Miniaturized atomic microsystems that are based on the laser cooling technique, which are the subject of ongoing research, have especially rigorous vacuum requirements: the chamber in which atoms are trapped and cooled requires ultrahigh vacuum (UHV) (i.e., at nTorr levels) in order to reduce the rate of spurious collisions between vapor phase atoms (e.g., rubidium) and background gas particles.[2–11] These collisions may perturb the trapped cold atoms, influencing measurement sensitivity and resolution. The conventional approach for providing UHV is to use extremely low leakage packaging with enclosed getters.[12–16] However, helium that permeates into all packages from the ambient atmosphere is not absorbed by typical getters, and this eventually compromises the vacuum.[17,18] This limits the useful life of devices, particularly when the vacuum cell is small in volume.

To sustain UHV conditions in miniature cells, one potential solution is the use of sputter-ion pumps.[17,19–23] Such pumps utilize crossed electric and magnetic fields in a Penning cell structure to trap electrons for ionizing the gases.[22,23] However, the electronic transition of trapped atoms in the atomic microsystems can be broadened through the Zeeman effect due to magnetic fields, resulting in inaccurate measurements.[24] Therefore, miniaturized magnet-less ion pumps are crucial for atomic clocks and atomic inertial measurement systems that require a stable UHV environment. One way to achieve the magnet-less gas pumping is by streaming high density electron current to result in a higher rate of ionization.[25,26] A previous effort proposed a high vacuum pump that increased the ion production by producing very large electron currents from field emitter arrays.[25] Another effort utilized a set of DC biased electrodes to modestly lengthen the trajectories of the field-emitted electrons.[26] However, these miniaturized ion pumps are dependent on a high current of field-emitted electrons that can lead to a significant pressure increase due to electron-induced gas desorption.[25,26] As an alternative, the miniaturized ion pump that is based on magnet-less electron spiraling

a)Electronic mail: kevindsy@umich.edu
b)Electronic mail: greensr@umich.edu
c)Present address: Sandia National Laboratory, Livermore, CA 94550; electronic mail: amarkos@sandia.gov
d)Electronic mail: mjkush@umich.edu
e)Electronic mail: yogesh@umich.edu

or oscillation can potentially require a much lower electron current while still generating a sufficient ionization rate. The primary challenge is to develop an appropriate magnet-less trapping technique that can still result in electron confinement while lengthening the trajectories by orders of magnitude, similar to the performance obtained with a Penning cell.

A radio frequency (RF) electron trap is proposed in this paper as a magnet-less electron trapping solution that can potentially fit within a miniaturized ion pump (Fig. 1). The RF electric fields serve as alternatives to crossed electric and magnetic fields to confine and cycle the electrons between two parallel electrodes in oscillating trajectories, as described below. This confinement extends the effective trajectory of the electrons. While demonstration of this magnet-less confinement concept is challenging, miniaturization of the RF electron trap structure presents further challenges. Primarily, the RF frequency that efficiently traps electrons scales inversely with the trap size, as does the dominant device capacitance. These scaling properties result in less efficient RF power transfer as the device is miniaturized, especially in terms of generating voltage sufficient for gas ionization. Other miniaturization challenges include dielectric breakdown of thinner insulation layers and more pronounced effects of fringe electric fields within a small volume.

The central elements of the proposed RF electron trap are two parallel grid electrodes that are separated by a prescribed distance to form the electron trapping region. The top grid electrode is powered by an RF voltage, and the bottom grid electrode is at ground potential. An external electron source supplies electrons that are trapped and energized by the RF field between the two grid electrodes.[27,28] This trapping greatly extends the trajectories of the electrons, which would otherwise terminate at the chamber walls. The extended trajectories increase the probability of ionizing collisions between the electrons and the neutral gas. This paper describes an electron trapping module (ETM) that experimentally demonstrates the RF electron trapping at the centimeter scale based on the conceptual structure shown in Fig. 1. This basic structure has been analytically and numerically modeled, and these results are discussed in Part I of this report.[29] Section II provides the details on the design and function of the ETM. Section III describes the experimental methods and results for electron trapping with the ETM, followed by discussion in Sec. IV and conclusions in Sec. V.

II. DESIGN AND FUNCTION

A. ETM concept and structure

The ETM utilizes a total of eight electrode elements in a multilayer, stacked architecture that can be easily reconfigured, thereby providing flexibility in the position, thickness, and composition of various elements (Figs. 2 and 3). All layers other than two perforated metal electrodes [Fig. 2(c)]—denoted RFA and RFB—possess the same U-shaped topography in the X-Z plane with a $1 \times 1\,cm^2$ opening. This opening permits the incoming electrons into the trap formed between the RFA and RFB electrodes and defines the cross-sectional area of the overall trapping region. The RFA and RFB electrodes are separated by a U-shaped metal element (Chassis) whose thickness determines the gap in which the electrons are to be trapped [Fig. 2(d)]. The stack is held together by screws using ceramic washers for electrical insulation. A U-shape is chosen for the device in this configuration to allow for direct probing of the electron trap through the opening in the U-shape. The effect of the asymmetry in this structure has not been fully measured, but modeling indicates that asymmetry on the edges of the structure do not strongly affect the performance in the central trapping region. Electrical isolation between each metal layer is realized by sandwiching U-shaped ceramic sheets [Fig. 2(b)] between the layers. This configuration enables rapid prototyping to explore the parameter space. For example, the gap between electrodes RFA and RFB can be simply changed by using a thicker Chassis. As another example, many perforated metal electrodes that have the same perforation pattern
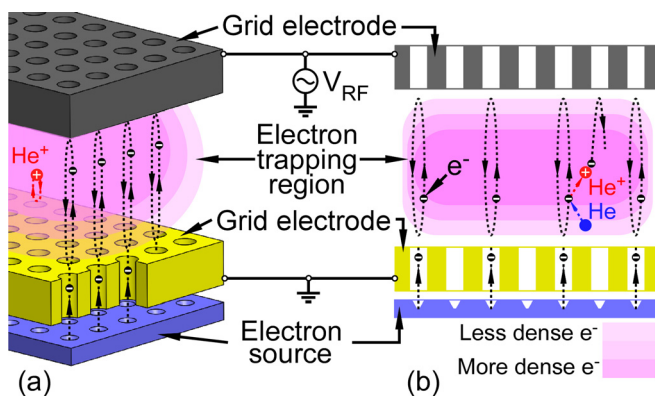

FIG. 1. (Color online) RF electron trap concept: 3D model (a) and 2D schematic (b). The RF electron trap mainly consists of two grid electrodes, which are separated by a certain distance to form an electron trapping region. Electrons are supplied by an external electron source. RF voltage is applied between the two grid electrodes to trap and energize the incoming electrons in the trapping region.
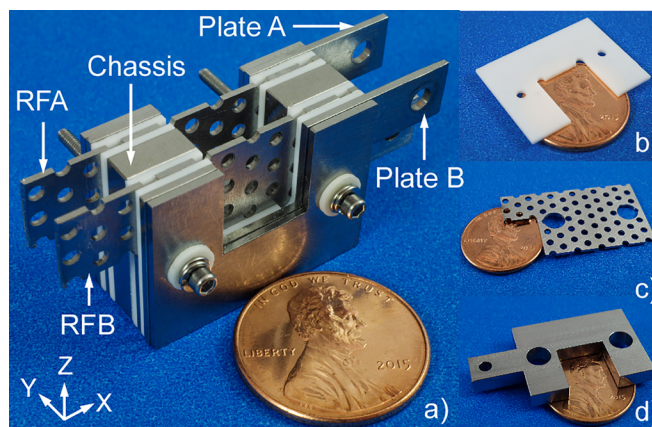

FIG. 2. (Color online) (a) ETM consists of two perforated stainless steel electrodes—RFA and RFB, separated by a U-shaped stainless steel Chassis with two U-shaped ceramic sheets for electrical isolation. (b) U-shaped ceramic sheet. (c) Perforated stainless steel electrode. (d) U-shaped stainless steel Chassis.

can be stacked to alter the effective aspect ratio of the perforations.

The metal layers are comprised of annealed type 304 stainless steel.[30] The ceramic layers are comprised of machinable Macor®—mica glass ceramic.[31] These materials exhibit low outgassing and are bakeable and hence are UHV compatible.[32,33] Additionally, these materials are not strongly magnetic.[30] All layers are machined using conventional processes (i.e., milling, drilling, etc.) and then cleaned by rinsing with acetone/isopropanol/deionized water prior to assembly. The RFA and RFB electrodes are machined from a 0.76 mm thick type 304 stainless steel sheet with a staggered pattern of 1.59 mm diameter holes; these electrodes have an open area of 40% to allow electrons to pass into the trapping area. These two electrodes are 19 mm wide and 40 mm long, including an extension used for electrical connection. Once the RFA and RFB electrodes are stacked, the perforations are well-aligned with a tolerance of ≈0.25 mm. The U-shaped ceramic layers (25.4 × 19 mm) are machined from 0.75 mm thick machinable ceramic Macor sheets, and two 1.70 mm diameter alignment holes are drilled. The Chassis is also made from a type 304 stainless steel sheet and trimmed down to 5.5 mm in thickness.

To experimentally diagnose the proposed RF electron trapping concept, five additional type 304 stainless steel electrodes are used: collector 1, collector 2, a cutoff electrode, and plates A and B, as shown in Figs. 3(a) and 3(b). Collector 1 in the X-Y plane covers the open side of the U-shaped stack that bounds the trapping region, whereas collector 2 covers the opening in the X-Z plane. Collector 1 is bolted to the stack. Collector 2 is clamped to the ceramic stand and is located opposite to the electron source. The perforated Cutoff electrode is sandwiched between electrodes RFB and plate B and isolated from both with ceramic layers. The perforation patterns of all three perforated electrodes (RFA, RFB, and cutoff) are well aligned (within ≈0.25 mm) to ensure that incoming electrons can pass into the trap. The cutoff electrode is the perforated electrode closest to the electron source; as such, it can be used if necessary to prevent the electrons from going into the trap by biasing it to a positive potential. Plates A and B are included to minimize the exposed surface area of the ceramic layers and thus reduce charge accumulation on the dielectrics. The ETM, without considering the two collectors and electrode extensions, is $2.5 \times 1.7 \times 1.9 \, cm^3$ in volume to enclose a $1.0 \times 1.0 \times 0.7 \, cm^3$ electron trap.

The electrical testing setup is shown in Fig. 3(c). Capacitors are placed in series with electrodes that are near the trapping region—RFA, collector 1, and Chassis—to provide DC isolation, while all other electrodes are grounded. These DC-isolated electrodes build up negative potentials—V_{Col1} at collector 1 and V_{Cha} at Chassis—that are related to the electron density in the trapping region.[34] Eventually, an equilibrium electron density is maintained in the trapping region after applying a specific RF signal between RFA and RFB, which establishes the steady state electrode potentials (SSEPs) for Collector 1 at V_{Col1_ss} and Chassis at V_{Cha_ss}. A high impedance 10:1 voltage divider is placed in parallel with the DC blocking capacitor to step down the electrode
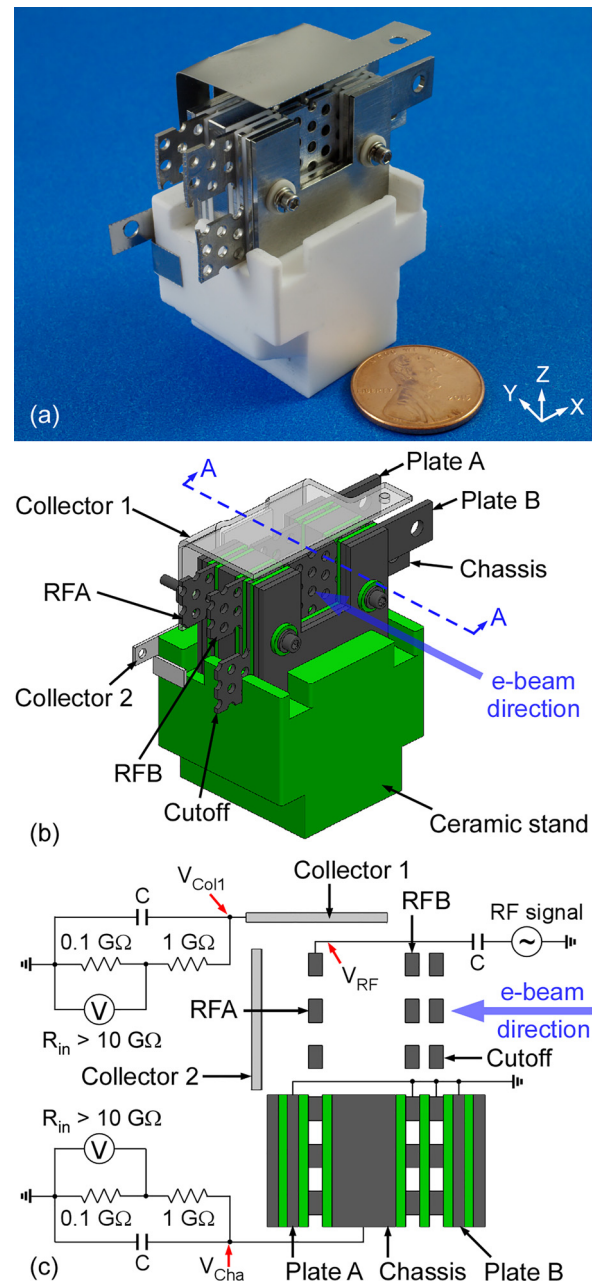

(a)

(b)

(c)

FIG. 3. (Color online) Testing setup. (a) The ETM assembled with three additional electrodes. (b) The 3D drawing of ETM. The ETM is electrically isolated and fixed in the position within the chamber by a ceramic stand. The electron beam is directed into the ETM with its spot size (20 mm) covering the Cutoff electrode. Collector 1 and collector 2 are used in diagnostic measurements. (c) Section A-A and electrical testing setup for RF electron trapping. DC blocking (AC passing) capacitors are added to Chassis and collector 1 electrodes. Another capacitor is added between the RF source and the RFA electrode.

potential; the reduced voltage is measured using a digital multimeter (Agilent 34401A). The input impedance of this multimeter (10 GΩ) substantially exceeds the impedance across which it is placed (0.1 GΩ). The overall impedance in parallel with the DC blocking capacitor is 1.1 GΩ, which is high enough to avoid shunting a significant electron current from the trap. In order to ensure that the placement of these capacitors does not significantly shift the series resonant frequencies of the device, relatively large capacitors (86 pF) are used.

B. Electrical characteristics

The behavior of the ETM at RF frequencies must be understood in order to estimate the RF voltage $|V_{RF}|$ generated across the grid electrodes for a given incident RF power P_{in}. For this characterization, all electrodes and the chamber are grounded except the RFA electrode, where the RF voltage is applied. A 60 cm long LMR-400 low loss RF coaxial cable is connected between the RFA electrode via the associated BNC electrical feedthrough and the impedance analyzer (Agilent 4395A). The impedance of the ETM along with the cable Z_{in} is measured, and the ETM impedance Z_L ["measured" impedance trace, Fig. 4(a)] is de-embedded by utilizing a lossless cable assumption and a lossless transmission line equation [Eq. (1) in Table I].[35]

A simplified equivalent circuit model [Fig. 4(b)] with seven series RLC branches in parallel from the RFA electrode to the ground is developed to represent the eight electrode elements in the ETM. For example, examining the RFB branch of the equivalent circuit model shows the capacitor C_{RFB} formed between the RFA and RFB electrodes. However, a stray resistance R_{RFB} and a stray inductance L_{RFB} are also present due to the unshielded wires in the vacuum chamber, the contact resistances of these wires, and the skin effect within the electrodes.[36] These parasitic components along with the capacitance cause a series resonant dip in the measured device impedance.

TABLE I. Equations for RF characterization (Refs. 35 and 37).

$$Z_{in}(f_{RF}) = Z_0 \frac{Z_L + jZ_0 \tan\left(\frac{2\pi f_{RF}L}{k_v c}\right)}{Z_0 + jZ_L \tan\left(\frac{2\pi f_{RF}L}{k_v c}\right)} \tag{1}$$

$$\Gamma = \frac{Z_L - Z_0}{Z_L + Z_0} \tag{2}$$

$$P_t = P_{in} \cdot (1 - |\Gamma|^2) \tag{3}$$

$$V_{L,peak} = \sqrt{2 P_t \cdot Z_L} \tag{4}$$

$$I_{RFB,peak} = \frac{V_{L,peak}}{R_{RFB} + j\left(2\pi f_{RF}L_{RFB} - \frac{1}{2\pi f_{RF}C_{RFB}}\right)} \tag{5}$$

$$|V_{RF}| = \frac{|I_{RFB,peak}|}{2\pi f_{RF}C_{RFB}} \tag{6}$$

Z_{in} = impedance measured along with the coax cable, Z_0 = characteristic impedance of the cable (50 Ω), L = length of the coax cable (0.69 m), c = speed of light, k_v = velocity of propagation for the LMR-400 cable (0.85), Γ = voltage reflection coefficient, P_t = RF power transmitted to the ETM, $V_{L,peak}$ = peak voltage across the ETM, and $I_{RFB,peak}$ = peak current through the RFB branch.
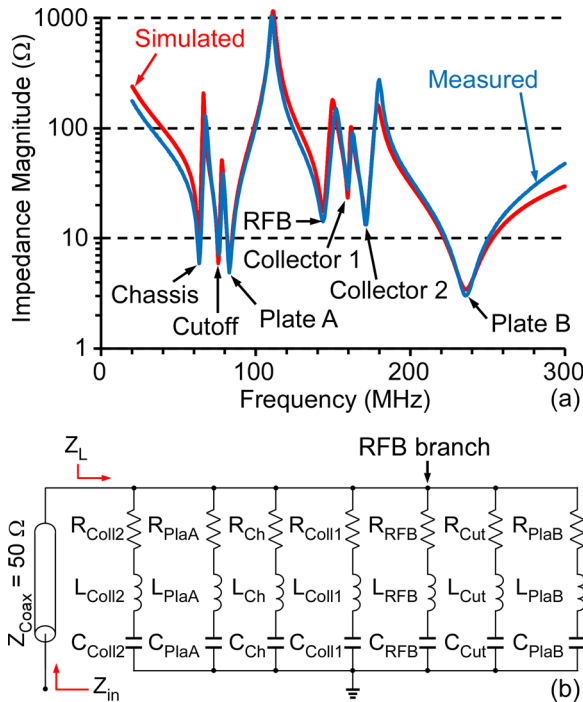
In order to assign the series resonant frequencies from the de-embedded impedance—the "measured" curve in Fig. 4(a)—to the correct branches of the equivalent circuit model, an experimental method is utilized. In this method, one branch at a time is loaded with an inductor (225 nH) between the electrode and the ground. A resulting shift of one of the series resonant dips in the measured (de-embedded) impedance is observed, indicating that the loaded branch is associated with that series resonant frequency. The process is repeated for each branch. In this way, series resonant frequencies of all seven branches can be identified.

The capacitances in each branch are first measured using a LCR meter (HP 4284A); these values are the beginning estimates for the capacitor in each branch. The inductance in each series RLC branch is determined by keeping the product of inductance and capacitance at a fixed value, which links to the series resonant frequency associated with that branch. The impedance at each series resonant frequency is then used to estimate the stray resistance of the associated branch since the reactance of the capacitor and the inductor in that branch are canceled out at series resonance. Then, the estimated values of inductances and capacitances are tuned together to match not only the series resonant dips but also the parallel resonant peaks in the de-embedded ETM impedance results. The values of all components in the equivalent circuit model are summarized in Table II. The SPICE simulated impedance of the ETM using this model ["simulated" impedance trace, Fig. 4(a)] is well aligned with the measured

FIG. 4. (Color online) (a) De-embedded ETM impedance magnitude $|Z_L|$ ("measured" curve) from the RFA electrode from 20 to 300 MHz with all electrodes except the RFA electrode grounded compared with the SPICE simulated $|Z_L|$ ("simulated" curve) from the equivalent circuit model of ETM. The de-embedded device impedance results suggest that the eight electrode elements in the device form parallel branches from the RFA electrode to the ground, each with a series resonant behavior. (b) The equivalent circuit model of the ETM.

TABLE II. Resonant frequencies and element values used in the equivalent circuit model.

Branch	Resonant frequency f (MHz)	Resistance R (Ω)	Inductance L (nH)	Capacitance C (pF)
Chassis	63.3	6.25	1210.00	5.23
Cutoff	75.9	6.25	916.90	4.80
Plate A	82.8	6.25	400.10	9.23
RFB	143.6	18.75	921.25	1.33
Collector 1	159.7	28.12	3103.75	0.32
Collector 2	171.5	15.63	747.50	1.15
Plate B	235.8	3.44	47.44	9.60

de-embedded ETM impedance ["measured" impedance trace, Fig. 4(a)]. This agreement indicates that the equivalent circuit model is an appropriate representation of the ETM. With this model, the actual $|V_{RF}|$ applied between electrodes RFA and RFB for a given P_{in} can be estimated by the $|V_{RF}|$ value appearing on C_{RFB} in the equivalent circuit model using Eqs. (2)–(6) (Table I).[37]

Using this model, the $|V_{RF}|$ value at the RFA electrode is calculated over the frequency range at different values of P_{in}, as represented by three curves ($P_{in} = 1.47$ W, $P_{in} = 0.37$ W, $P_{in} = 0.09$ W) in Fig. 5. The calculated $|V_{RF}|$ value peaks for any given value of P_{in} at the series resonant frequency of the RFB branch (143.6 MHz). As electrons enter the trap, these electrons are subjected to the oscillating Lorentz force driven by the RF electric field. This force causes the electrons to oscillate between the RF electrodes. In Ref. 29, an electron trapping confinement factor k_{trap} is defined to indicate the confinement of trapped electrons

$$k_{trap} = \sqrt{\frac{2m_e}{|V_{RF}|q}} \pi f_{RF} d, \qquad (7)$$

where m_e is the mass of an electron, q is the fundamental charge, and d is the gap between electrodes RFA and RFB. When the values of $|V_{RF}|$, f_{RF}, and d in Eq. (7) result in a k_{trap}
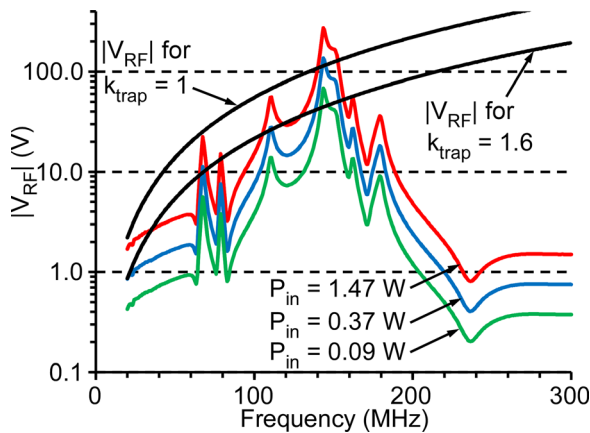

FIG. 5. (Color online) Three curves indicate peak RF voltage $|V_{RF}|$ developed at the RFA electrode across the frequency range under different P_{in} values (1.47 W, 0.37 W, and 0.09 W). The $|V_{RF}|$ values vs frequency are plotted for k_{trap} values of 1 and 1.6 [Eq. (7)].

value of 1, the oscillating trapped electrons travel the entire gap between electrodes RFA and RFB during each cycle, which is considered an optimal trap. The voltage amplitude for $k_{trap} = 1$ is denoted as $|V_{RF}^*|$. The calculated $|V_{RF}^*|$ value for this 7 mm gap device over the frequency range of 20–300 MHz is indicated by the $k_{trap} = 1$ curve in Fig. 5. No RF electron trapping is expected to exist when the RFA electrode is operated with $|V_{RF}| > |V_{RF}^*|$, as electrons will be accelerated beyond the trap before the voltage can cycle to keep them in the trap. In this case, k_{trap} is less than 1. With $|V_{RF}|$ lower than $|V_{RF}^*|$, or $k_{trap} > 1$ equivalently, RF trapping is expected to exist with tighter confinement, as the excursion of trapped electrons will be reduced to only a portion of the electrode gap (example voltages for this case are the $|V_{RF}|$ values indicated by the $k_{trap} = 1.6$ curve in Fig. 5). By substituting the calculated $|V_{RF}^*|$ value at a f_{RF} value of 143.6 MHz into Eq. (6) from the equivalent circuit model, the required P_{in} value to initiate this optimum RF electron trapping can be determined. The calculated optimum operating RF signal for the 7 mm gap ETM is at a f_{RF} value of 143.6 MHz and a P_{in} value of 0.836 W. Note that only a portion of the P_{in} is transmitted to the device, while the remainder is reflected back to the source; this power transmission efficiency can be improved with an appropriate matching network or RF transformer.

III. EXPERIMENTAL METHODS AND RESULTS

All RF electron trapping tests were performed using a steady emission current of 40 μA and an electron energy of 15 eV. The emission current was provided by an electron gun (Kimball Physics, FRA-2X1-2) and controller. The test chamber, described in the Appendix, was maintained at 70 nTorr for all the tests.

The recorded reference SSEP across the DC blocking capacitors with only the presence of the electron beam was −13.5 V at both collector 1 (V_{Col1_rss}) and Chassis (V_{Cha_rss}). No major shifts of V_{Col1_rss} and V_{Cha_rss} were found throughout the course of testing. The testing sequence of RF electron trapping experiments is indicated by the subscripts in the results, and the repeatability of testing results is indicated by the error bars at different power levels.

The recorded V_{Col1_ss} and V_{Cha_ss} values as a function of RF power at a f_{RF} value of 143.6 MHz are shown in Fig. 6. At a P_t value of 0.033 W (P_{in} of 0.105 W), V_{Col1_ss} was −15.9 V, while V_{Cha_ss} was −20.8 V; both the values were more negative than the recorded V_{Col1_rss} and V_{Cha_rss} value. As P_t increased to 0.130 W (P_{in} of 0.419 W), V_{Col1_ss} increased to −13.0 V, and V_{Cha_ss} was −13.1 V; both the values were close to the recorded V_{Col1_rss} and V_{Cha_rss} value. Further, V_{Col1_ss} was −13.2 V, and V_{Cha_ss} was −5.5 V at a P_t value of 0.517 W (P_{in} of 1.668 W); both V_{Col1_ss} and V_{Cha_ss} became more positive than the V_{Col1_rss} and V_{Cha_rss} value.

The dependence of V_{Col1_ss} and V_{Cha_ss} on RF frequency is shown in Fig. 7. Based on five testing points in the frequency range of 141 to 152.5 MHz at a fixed P_{in} value of 0.836 W (at 143.6 MHz, this is calculated as P_t of 0.259 W),
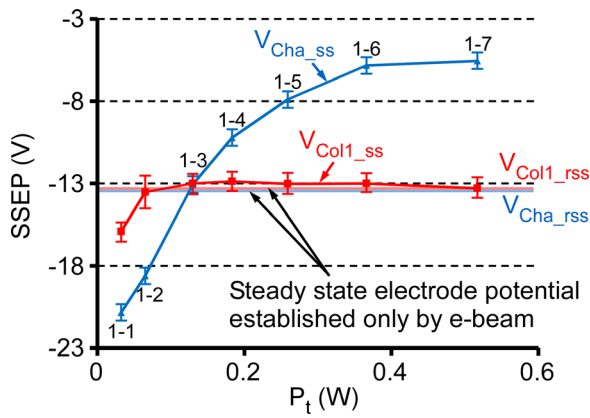
FIG. 6. (Color online) V_{Col1_ss} and V_{Cha_ss} measured during RF electron trapping at different powers transmitted to the ETM and P_t with a fixed f_{RF} value of 143.6 MHz. The horizontal lines represent the recorded V_{Col1_rss} and V_{Cha_rss} with only the injection of the 40 μA electron beam.

V_{Cha-ss} ranged from -7.4 to -6.2 V and V_{Col1_ss} ranged from -13.1 to -12.0 V. The change in V_{Col1_ss} and V_{Cha_ss} over the investigated frequency range was approximately 10%.

IV. DISCUSSION

The V_{Col1_ss} and V_{Cha_ss} values are more negative than V_{Col1_rss} and V_{Cha_rss} at a P_t value of 0.033 W (P_{in} = 0.105 W), which implies that the electron density in the trapping region increases by the application of the RF voltage, as is consistent with the design expectations. The more negative potentials measured at these electrodes when RF voltage is applied denote larger thermal electron current through the resistor networks connected to the electrodes. This larger thermal electron current is available only from the higher electron density near the electrodes. Furthermore, V_{Cha_ss} is more negative than V_{Col1_ss}. This result further supports the conclusion that a more negative electrode potential corresponds to a higher electron density, for the following reasons. The U-shaped metal Chassis, sandwiched by the RFA and RFB electrodes, has three sides immediately
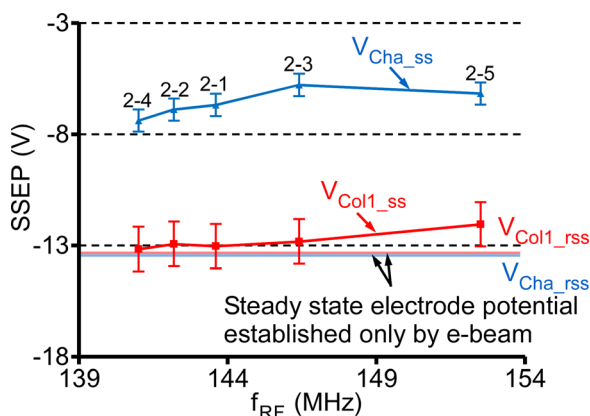

FIG. 7. (Color online) V_{Col1_ss} and V_{Cha_ss} measured during RF trapping at different f_{RF} value with a fixed P_{in} value of 0.836 W (P_t of 0.259 W at 143.6 MHz). The horizontal lines represent the recorded V_{Col1_rss} and V_{Cha_rss} with only the injection of the electron beam.

adjacent to the RF electron trapping region, while collector 1 only covers the remaining side of the trap and is $\approx$3 mm further away from the trap. Thus, the Chassis is physically closer to the trapping region and has more area surrounding the electron trap than collector 1. The physical proximity to the region of higher electron density and the larger surface area of the Chassis accesses more electron current, leading to a more negative potential on the Chassis.

The use of the steady-state DC potentials on these electrodes, rather than any RF or other rapidly changing voltages, is an important aspect of the measurement technique. The vast difference in time scales between when these potentials are measured (minutes after the application of RF power) and the period of the RF cycle (nanoseconds for each cycle) helps to separate the changes in potential due to the local, RF driven electron movement from those changes due to the thermal drift and diffusion of the electrons. The slower thermal drift and diffusion processes are more indicative of average electron density and are more properly measured with the steady state DC potential established on the electrodes.

While the diagnostic approach utilized here is simple and adequate for semiquantitative assessment of the trapping concept, improvement of the approach or utilization of other diagnostic methods warrants investigation in future assessment and refinement of the RF traps. The approach utilized here can be improved in the future with an appropriate redesign: rather than relying on the Chassis or Collector surfaces that are necessarily at the periphery of the trapping volume, a needlelike probe can be positioned near the center of the trapping volume. Utilizing a very small probe in this location will minimally disturb the electric fields and RF behavior of the device, while also providing the most sensitivity to the location of the largest electron density within the trapping volume. An important constraint on the size of the probe is that it should minimize perturbations of the plasma and electric fields. The recommended probe size depends on the mean free path of the gas and can be larger at the low pressures used in this device.[38] In principle, microfabricated Langmuir probes can be incorporated with an appropriate redesign.[39,40] Although optical techniques such as interferometry and Stark broadening have been used to estimate plasma densities, these techniques would be extremely challenging in the compact, very low density plasmas created by this device.

A plasma transport model[41] was extended and used to analyze the ETM SSEP testing, and this process is described in Part I.[29] This model was used to estimate the electron distribution as well as the potentials at capacitively isolated electrodes while operating at different RF voltage levels. For a $|V_{RF}|$ value of 150 V at the RFA electrode and an f_{RF} value of 150 MHz as shown in Fig. 8, modeling results show 3–4 orders of magnitude increase in electron density in the trapping region. In addition, the simulated SSEPs at this RF voltage level are more negative than the simulated reference SSEPs with only the presence of the electron beam. These results support the premise that higher electron density results in a more negative SSEP.
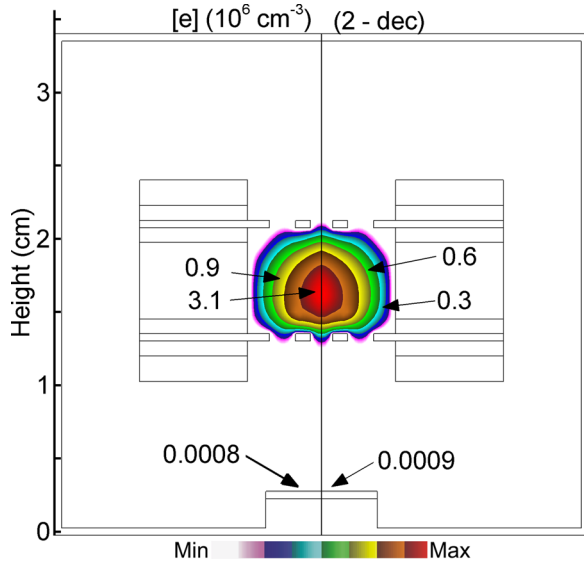
FIG. 8. (Color online) Simulated electron density based on a plasma transport model (He, 80 nTorr, 150 MHz, 150 V, 15 eV initial electron energy, and 40 μA electron current from source). Densities are plotted on a 2-decade log scale with the maximum values indicated (Ref. 29).

FIG. 9. Simulated maximum electron densities as a function of applied RF voltage at 150 MHz (He, 80 nTorr, 15 eV, 40 μA) (Ref. 29).

It should be noted that these negative SSEPs peak at a RF power level—P_t of 0.033 W ($P_{in} = 0.105$ W)—lower than the estimated optimum RF power level—P_t of 0.259 W ($P_{in} = 0.836$ W). The most likely cause of this is the nonideality of the electric fields resulting from the perforated electrodes. The relatively large perforations result in lateral fringing fields near the electrodes and extending into a significant portion of the trap volume. The optimum power level is estimated from a simple model that does not account for these lateral fields and is termed optimal because it would allow the entirety of the trap volume to be utilized. However, the existence of the lateral fringing fields effectively reduces the usable trap volume, and thus, a lower voltage (resulting in a higher k_{trap} and a reduced electron excursion) at a lower power level more optimally densifies the electrons in this case.

As P_t increases in Fig. 6, V_{Col1_ss} and V_{Cha_ss} become more positive, indicating a less efficient trap. With a further increase in the P_t value, V_{Col1_ss} and V_{Cha_ss} become more positive than V_{Col1_rss} and V_{Cha_rss}. This indicates a smaller electron density in the trapping region due to the applied RF signals. Both these observations are expected from Eq. (7).[29] As $|V_{RF}|$ becomes larger than $|V_{RF}^*|$, the incoming electrons are accelerated excessively and leave the trap before the voltage can cycle and keep the electrons in the trap. Therefore, the trends in Fig. 6 indicate that the most effective electron trapping occurs over a small range of RF power. RF power outside this range results in reduced electron trapping. The peak electron density inside the trap predicted by the model described in Part I (Ref. 29) over a range of $|V_{RF}|$ applied for a f_{RF} value of 150 MHz indicated a similar small range of trapping potentials (Fig. 9).

The charge density in the trap is small and may be below the ambipolar limit, and so, charge neutrality is not strictly required. Even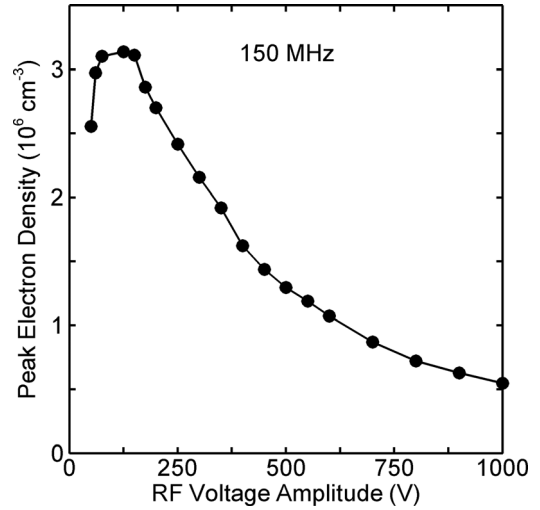 so, assuming that the trapped electron density is equal to the ion density to maintain the zero net charge in the trapping region, and all ions are helium ions, the electron current equation for a planar probe with a collisionless sheath can be used to estimate the electron density near the capacitively isolated electrodes (Chassis and collector 1).[42] The electron current in the original equation is calculated from the recorded steady state electrode potential V_p divided by the 1.1 GΩ resistor in parallel with the DC blocking capacitors. After simplification

$$n_e \approx -1.4 \times 10^4 \cdot V_p \, \mathrm{cm}^{-3}, \tag{8}$$

where V_p (in volts) is either V_{Col1_ss} or V_{Cha_ss} and n_e is the estimated electron density. The estimated electron density is $3 \times 10^5 \, \mathrm{cm}^{-3}$ near the Chassis at a P_t value of 0.033 W and a f_{RF} value of 143.6 MHz, which agrees well with the simulated electron density near the edge of the trap as shown in Fig. 8.[29] Note that this simplified relation is only expected to be valid for a very limited range of operating conditions. The simulation results presented here and in Ref. 29 are expected to be valid over a larger range of operating conditions, as the numerical modeling makes no assumptions about charge neutrality, accounts for nonideal electric fields, and incorporates the effects of charge accumulation on dielectric surfaces.

The values of V_{Col1_ss} and V_{Cha_ss} remain flat over the tested frequency range in Fig. 7, indicating that the electron density within the trap is similar over a range of f_{RF} at approximately the same power level. Similarly, the simulated peak electron densities are relatively insensitive to frequency and can occur over a fairly broad k_{trap} region as indicated in the numerical modeling in Part I.[29]

As suggested by the results from the ETM, improvements can be implemented in the future designs to achieve better electron trapping performance. First, finely perforated RF electrodes are preferable because the finer perforations result in lateral fringing fields that occupy much less of the trap volume. Then, parasitic resistances and capacitances of the

device can be optimized by reducing unused electrodes, reducing the volume and the exposed surface area of the ceramics, and improving skin effect losses. The reduction in parasitic resistances and capacitances will effectively improve the quality factor of the series resonance of the device, which should significantly reduce the power consumption.

There are additional requirements to be met for demonstrating a full miniaturized magnet-less ion pump. An electron source, such as a field emitter array, should be integrated.[27,28] Ideally, the perforations of the grid electrodes would align with the tips of such an array to efficiently pass the electrons into the trapping area. The dead volume of the trapping device should be further minimized, resulting in a higher trap-to-device volume ratio, which will lower the gas load imposed by the trap. In addition, it must be demonstrated that the RF electric field can not only trap more electrons but also maintain the electron kinetic energy above the ionization threshold to promote gas ionization. Finally, a pulsed DC scheme for accelerating and burying the ionized gas molecules must be demonstrated.

V. CONCLUSION

This work demonstrated that magnet-less RF-based electron traps are viable at subcubic centimeter scales. The trap utilizes RF electric fields to oscillate electrons in the trapping volume ($0.7 \, cm^3$) between two perforated electrodes. A measurement technique was identified to estimate the efficiency of RF electron trapping. This technique is based on measuring steady state potentials on electrodes near the trap and correlating those values with thermal electron current and electron density within the trap. At a P_t value of $0.033 \, W$ for $f_{RF} = 143.6 \, MHz$, the measured SSEPs at Chassis and collector 1 were more negative than reference SSEPs with RF power off due to only the injection of the electron beam. These results are consistent with the premise that the electron density over the trapping region was increased by the applied RF signal, up to a calculated value of $\approx 3 \times 10^5 \, cm^{-3}$ near the walls of the trapping region. In accordance with analytical and numerical modeling, larger RF power levels indicated a lower electron density (calculated as low as $\approx 1 \times 10^5 \, cm^{-3}$ near the walls of the trapping region) and demonstrated that effective RF electron trapping only occurs over a certain RF power range at a specific RF frequency. The miniaturized RF electron trap described here addresses the challenges of magnet-less electron confinement and RF power transfer in a miniaturized device and may enable magnet-less ion pumping solutions that will significantly increase the operating lifetime of extremely accurate atomic microsystems in development.

ACKNOWLEDGMENTS

APPENDIX: EXPERIMENTAL SETUP

The experimental setup is configured to provide the vacuum environment and electron source for testing the RF electron trapping (Fig. 10). The pumps are connected to the vacuum chamber (Kimball Physics, 2.75 in. Double Spherical Cube Vacuum Chamber) through a tee connector and individual manual isolation valves: an all-in-one turbo pump (Agilent, Mini-TASK AG81), capable of pumping down to $<100 \, nTorr$, and a sputter ion pump (Agilent, 20 l/s VacIon Pump), capable of pumping down to 0.1 nTorr. One valve (Kurt J. Lesker, 2.75 in. CF Manual Bellows Sealed SS Angle Valves) is attached to the chamber for venting, and the other valve (Agilent, Variable Leak Valve) is attached for leaking in small amounts of gas, e.g., helium. The pressure inside the chamber is continuously monitored by an ion gauge (Adixen, AHC 2010). One BNC electrical feedthrough (Kurt J. Lesker, 2.75 in. CF 4xBNC) and another SHV electrical feedthrough (Kurt J. Lesker, 2.75 in. CF 4xSHV) are connected to the chamber to provide electrical access to all metal layers of the ETM. An electron gun (Kimball Physics, FRA-2X1-2 Electron Gun) with an insertion length of 150 mm serves as the electron source for the RF electron trapping testing. The electron gun is offset by 58.74 mm with a custom 2.75 in. CF full nipple from the right side of the chamber, such that the tip of the cathode barrel for the electron gun is 10.7 mm away from the opening of the ETM. This separation is close to the minimum working distance for this electron gun and maximizes the percentage of the emitted electrons arriving at the trapping region. Several customized stands are used to mechanically support the setup and to adjust the relative position of the different components.

The ETM is placed on a customized Macor stand for electrical isolation from the grounded chamber [Fig. 3(a)]. The ceramic stand is fixed by two 2.75 in. Groove Grabbers (Kimball Physics, MCF275-GrvGrb-C02). It is located in the
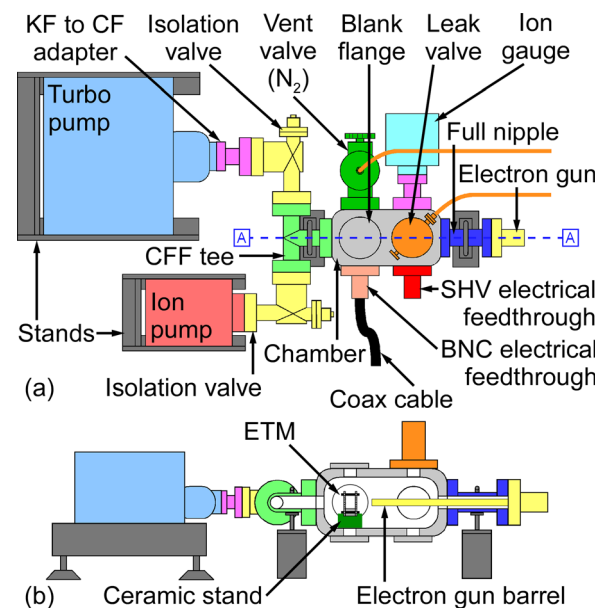

FIG. 10. (Color online) Experimental vacuum setup. (a) Top view. (b) A-A sectional view.

left part of the chamber close to the BNC electrical feedthrough. The trap opening is perpendicular to and centered on the tip of the electron gun barrel. The large arrow in Fig. 3 indicates the incoming direction of the electron beam.

The RFA, RFB, and cutoff electrodes and Chassis are electrically connected via the 50 Ω BNC electrical feedthrough with minimum lengths of solid core wires (Fig. 10). The intention here is to reduce the parasitic inductances and capacitances at RF frequencies. Collector 1, collector 2, plate A, and plate B electrodes are electrically connected to the SHV electrical feedthrough via solid core wires. This feedthrough can accommodate high voltage ($>1\,kV$) DC and pulsed DC signals.

[1] J. Zook, D. Burns, H. Guckel, J. Sniegowski, R. Engelstad, and Z. Feng, Sens. Actuators, A **35**, 51 (1992).

[2] C. Borde, Metrologia **39**, 435 (2002).

[3] S. Knappe, "MEMS atomic clocks," in *Comprehensive Microsystems*, edited by Y. B. Gianchandani, O. Tabata, and H. Zappe (Elsevier, Oxford, 2008), Chap. 3.18, pp. 571–612.

[4] P. D. D. Schwindt, Y. Y. Jau, H. Partner, A. Casias, A. R. Wagner, M. Moorman, R. P. Manginell, J. R. Kellogg, and J. D. Prestage, Rev. Sci. Instrum. **87**, 053112 (2016).

[5] R. Lutwak *et al.*, *36th Annual Precise Time and Time Interval (PTTI) Meeting* (2004), pp. 339–354.

[6] Y. Y. Jau, H. Partner, P. D. D. Schwindt, J. D. Prestage, J. R. Kellogg, and N. Yu, Appl. Phys. Lett. **101**, 253518 (2012).

[7] D. R. Scherer *et al.*, *46th Annual Precise Time and Time Interval Systems and Application Meeting* (2014), pp. 154–163.

[8] K. Nelson, K. Salit, J. Kriz, D. Sandquist, and J. Sebby-Strabley, *2012 IEEE/ION Position Location and Navigation Symposium (PLANS)* (2012), pp. 1094–1098.

[9] T. Müller, M. Gilowski, M. Zaiser, P. Berg, C. Schubert, T. Wendrich, and E. M. Rasel, Eur. Phys. J. D **53**, 273 (2009).

[10] B. Canuel, F. Leduc, D. Holleville, A. Gauguet, A. Virdis, A. Clairon, and P. Bouyer, Phys. Rev. Lett. **97**, 010402 (2006).

[11] J. Kitching, S. Knappe, and E. Donley, IEEE Sens. J. **11**, 1749 (2011).

[12] G. Wu, D. Xu, B. Xiong, Y. Wang, and Y. Ma, J. Microelectromech. Syst. **21**, 1484 (2012).

[13] L. Mauri, E. Rizzi, M. Moraja, and M. Campaniello, *2013 Microelectronics Packaging Conference (EMPC)* (2013), pp. 1–4.

[14] D. Sparks, N. Najafi, and B. Newman, U.S. patent 7,789,949 (7 September 2010).

[15] D. Sparks, N. Najafi, and S. Massoud-Ansari, IEEE Trans. Adv. Packag. **26**, 277 (2003).

[16] A. Dellis, V. Shah, E. Donley, S. Knappe, and J. Kitching, Opt. Lett. **41**, 2775 (2016).

[17] G. L. Saksaganskii, *Getter and Getter-Ion Vacuum Pumps* (Harwood Academic, Amsterdam, 1994).

[18] B. Kim *et al.*, J. Appl. Phys. **105**, 013514 (2009).

[19] S. A. Wright and Y. B. Gianchandani, J. Vac. Sci. Technol., B **25**, 1711 (2007).

[20] S. R. Green, R. Malhotra, and Y. B. Gianchandani, J. Microelectromech. Syst. **22**, 309 (2013).

[21] T. Grzebyk, A. Górecka-Drzazga, and J. A. Dziuban, Sens. Actuators, A **208**, 113 (2014).

[22] M. Audi and M. de Simon, Vacuum **37**, 629 (1987).

[23] K. M. Welch, *Capture Pumping Technology*, 2nd ed. (Elsevier, Amsterdam, 2001).

[24] J. A. Rushton, M. Aldous, and M. D. Himsworth, Rev. Sci. Instrum. **85**, 121501 (2014).

[25] A. A. Fomani, L. F. Velásquez-García, and A. I. Akinwande, *Technical Digest of 27th International Vacuum Nanoelectronics Conference (IVNC)* (2014), pp. 210–211.

[26] A. Basu and L. F. Velásquez-García, J. Micromech. Microeng. **26**, 124003 (2016).

[27] C. A. Spindt, C. E. Holland, A. Rosengreen, and I. Brodie, IEEE Trans. Electron Devices **38**, 2355 (1991).

[28] L. F. Velásquez-García, B. L. P. Gassend, and A. I. Akinwande, J. Microelectromech. Syst. **19**, 484 (2010).

[29] A. H. Markosyan, S. R. Green, S. Deng, Y. B. Gianchandani, and M. J. Kushner, "Miniaturized magnet-less RF electron trap: I. Modeling and analysis," J. Vac. Sci. Technol. B **35**, 042001 (2017).

[30] "Stainless steel—Grade 304 (UNS S30400)," accessed October 2016, http://www.azom.com/article.aspx?ArticleID=965.

[31] "Macor," accessed October 2016, http://glassfab.com/wp-content/uploads/2015/08/Corning-Macor.pdf.

[32] "A compilation of outgassing data on vacuum materials," accessed October 2016, http://ncsx.pppl.gov/NCSX_Engineering/Materials/VacuumMaterials/Outgassing_Data.pdf.

[33] S. Sgobba, CERN Technical Specification, No. 004 (2006), pp. 117–143.

[34] M. Sugawara, *Plasma Etching: Fundamentals and Applications* (Oxford University, New York, 1998).

[35] C. Qian and W. W. Brey, J. Magn. Reson. **199**, 104 (2009).

[36] W. H. Hayt and J. A. Buck, *Engineering Electromagnetics*, 8th ed. (McGraw-Hill, New York, 2011).

[37] I. S. Grant and W. R. Phillips, *Electromagnetism*, 2nd ed. (Wiley, West Sussex, 1991).

[38] V. A. Godyak, R. B. Piejak, and B. M. Alexandrovich, Plasma Sources Sci. Technol. **11**, 525 (2002).

[39] F. C. Chiang, P. Pribyl, W. Gekelman, B. Lefebvre, L. Chen, and J. W. Judy, IEEE Trans. Plasma Sci. **39**, 1507 (2011).

[40] E. F. C. Chimamkpam, E. S. Field, A. I. Akinwande, and L. F. Velasquez-Garcia, J. Microelectromech. Syst. **23**, 1131 (2014).

[41] M. J. Kushner, J. Phys. D **42**, 194013 (2009).

[42] M. A. Lieberman and A. J. Lichtenberg, *Principles of Plasma Discharges and Materials Processing* (Wiley, Hoboken, 1994).